

Ground-Based Passive Microwave Profiling during Dynamic Weather Conditions

K. Knupp¹, R. Ware^{2,4}, D. Cimini^{3,5}, F. Vandenberghe⁴, J. Vivekanandan⁴,
E. Westwater⁵, T. Coleman¹, and D. Phillips¹

¹University of Alabama in Huntsville (UAH), Huntsville, AL 35805

²Radiometrics Corporation, 2840 Wilderness Place
Boulder, CO 80301-5414, 303 449-9192

³Center of Excellence CETEMPS, University of L'Aquila, Coppito, 67010 L'Aquila, Italy

⁴National Center for Atmospheric Research, Boulder, CO 80307

⁵Cooperative Institute for Research in the Environmental Sciences, University of Colorado/
NOAA Environmental Technology Laboratory, Boulder, CO 80305

¹Corresponding Author: Department of Atmospheric Science, University of Alabama in Huntsville,
Huntsville, AL 35805; kevin.knupp@nsstc.uah.edu

Submitted to *J. Atmos. Oceanic Tech.*

March 2008

ABSTRACT

Short period (1-5 min) temperature and humidity soundings up to 10 km height are retrieved from ground-based 12-channel microwave profiling radiometer (MPR) observations. In contrast to radiosondes, the radiometric retrievals provide high temporal resolution (one minute or less) of thermodynamic profiles, but the vertical resolution, which declines in proportion to the height above ground level, is lower. The high temporal resolution is able to resolve detailed meso- γ scale thermodynamic and limited microphysical features of various rapidly changing mesoscale and/or hazardous weather phenomena. To illustrate the MPR capabilities and potential benefits to research and operational activities, we present example radiometric retrievals from a variety of dynamic weather phenomena including upslope supercooled fog, snowfall, a complex cold front, a nocturnal bore, and a squall line accompanied by a wake low and other rapid variations in low-level water vapor and temperature.

1. Introduction

The thermodynamic state of atmospheric conditions above the surface has been traditionally probed at synoptic-scale spacing twice daily by radiosondes, which provide vertical profile information needed for weather diagnosis and prediction. However, widely-spaced twice-per-day soundings do not resolve the temperature and humidity changes associated with most microscale and mesoscale phenomena, which evolve on temporal scales of minutes to hours, and have spatial scales of 1-10 km. The high-frequency sampling of thermodynamic profiles promotes understanding of complex mesoscale phenomena, and is likely a prerequisite to improvements in weather prediction. Although GOES and polar orbiting satellite infrared sounders have potential to provide thermodynamic profile measurements (e.g., Chahine et al 2006, Zhou et al. 2007), they are limited by relatively crude vertical resolution at lower levels within the important atmospheric boundary layer and/or by the presence of optically thick clouds. Continuous ground-based radiometric profiler observations can be used to fill the temporal gaps between radiosonde soundings. Although ground-based infrared sounding systems show promise (Feltz et al. 2003), microwave radiometers have a broader capability, and can generally provide profiles during cloudy and light-precipitating conditions. A more general description of ground-based radiometric profiling of temperature and water vapor is provided by Westwater (1993), and experimental results from a 6-channel radiometer are discussed by Hogg et al. (1983).

We present examples of radiometric retrievals for a variety of mesoscale weather systems sampled at Boulder, Colorado and Huntsville, Alabama. Dynamic weather conditions include

⁵ The UAH MPR was upgraded in 2005 with a more powerful blower and hydrophobic radome to mitigate emission from a wet radome.

supercooled fog and snowfall at Boulder, as well as a bore, complex cold front, and intense squall line from Huntsville.

2. Radiometer characteristics and other data

a. Radiometer characteristics

The Radiometrics 12-channel microwave profiling radiometer (MPR) observes atmospheric brightness temperatures in 5 frequency bands from 22 to 30 GHz, and in 7 bands from 51 to 59 GHz (Solheim et al., 1998; Ware et al. 2003). It also measures zenith infrared temperature, and surface temperature, humidity and pressure. The radiometer has automated elevation and (an optional) azimuth scanning capability, and the observation interval in the current instruments can be as short as 10 seconds. The antenna beam width ranges from 2° at 59 GHz to 6° at 22 GHz. The instrument is portable, with 0.12 m³ volume and 32 kg weight. Historical radiosonde records and neural network or regression algorithms are used to retrieve temperature and humidity profiles up to 10 km height, and low-resolution cloud liquid profiles (Solheim et al 1998).

Errors typically assigned to radiosonde data, when assimilated into numerical weather models, are shown in Fig. 1. The *representativeness* error resulting from characterization of a model cell volume by the radiosonde point measurement is dominant. Also shown in Fig. 1 are radiometric retrieval errors determined from statistical comparisons with radiosondes at mid-latitude and arctic sites (Güldner and Spänkuch 2001; Liljegren 2001). Retrievals based on regression algorithms are shown. The radiometric retrievals are based on volumetric measurements at zenith, and are less susceptible to representativeness error than radiosonde soundings. For temperature retrievals, the error is smaller than the radiosonde error in the boundary layer and is slightly higher above the boundary layer. The maximum RMS

temperature error is 2 K at 10 km. The water vapor density retrieval RMS errors exhibit a maximum of 1 g m^{-3} at 2 km AGL, and are smaller than radiosonde errors at all heights. The effective resolution of the MPR scales with height; in general, accurate profiles of each are obtained over the lowest 3 km (e.g., Westwater et al. 2000, Guldner and Spänkuch 2001).

For the Boulder examples, MPR measurements were acquired at 5-minute intervals, while the Huntsville radiometer sampled with a one-minute period. Thermodynamic retrievals at both locations were obtained using neural network methods.

c. Measurements from Huntsville

The University of Alabama in Huntsville (UAH) maintains a cluster of profiling instruments, including a MPR of the type described in the previous subsection. The temperature and water vapor density data have been transformed to potential temperature and water vapor mixing ratio, both of which are conserved for subsaturated adiabatic motions. Other instruments include a 915 MHz Doppler wind profiler, a 2 kHz Doppler sodar, a lidar ceilometer (0.905 μm), and surface instrumentation, all located at the UAH profiling site on campus. When in mobile form, these instruments comprise the UAH Mobile Integrated Profiling System (MIPS, see <http://vortex.nsstc.uah.edu/mips/> for details). The Advanced Radar for Meteorological and Operational Research (ARMOR, a C-band dual-polarimetric radar) is located 14 km to the southwest, and another Doppler radar and GPS radiosonde system are located on Redstone Arsenal, 14 km to the south.

3. Measurements

The diversity of radiometric measurements is illustrated with five contrasting examples presented in the following subsections. These cases include measurements from an upslope supercooled fog event and snow event in Boulder; and a bore, complex cold front, and squall line in Huntsville.

a. Upslope with supercooled fog

Prolonged upslope weather conditions occurred in the Denver area from 14 to 17 February 2001. An initial cold frontal passage occurred early on 14 February. A secondary cold front with a larger, colder, and more intense trailing anticyclone reinforced the upslope flow around Denver on 16-17 February. Radiometric retrievals up to 2 km AGL (ground level is about 1.5 km MSL at Boulder) on 16 February 2001 are shown in Fig. 2. Advection of cold air behind the secondary cold frontal surge produced shallow moist upslope conditions along the Front Range, beginning near 1045 UTC on 16 February. The passage of this front is represented as a modest 3 °C decrease in surface temperature (Fig. 3a) and a 15% increase in surface relative humidity (Fig. 3b) during the 1-h period following the frontal passage. The radiometric retrievals shown in Figs. 2a and 2b clearly show that the frontal passage was confined to levels below about 500 m AGL, where the cold, moist air is most prominent.

Clear conditions prior to and just after the frontal passage were followed by a rapid onset of fog at 1140 UTC, as indicated by the step increase in infrared temperature to 265 K by 1150 UTC (Fig. 3b). Integrated cloud water (Fig. 3d) reached a maximum of 0.26 mm near 1715 UTC. The corresponding maximum value of retrieved cloud water density was around 0.6 g m⁻³ at 300 m AGL when the depth of the cold, moist air was near a maximum. The presence of fog is substantiated by the near equality in infrared temperature and actual air temperature, both

measured at about 265 K. Thus, the fog was supercooled, with a mean temperature over the 500 m depth of the fog layer of about -8 °C. The integrated water vapor retrieval (Fig. 3c) shows a steady increase from 5.1 mm at the time of frontal passage to 6.5 mm near 2000 UTC. The radiometer rain sensor (not shown) did not indicate liquid precipitation accumulation during this period.

A comparison of the radiometer sounding with the 1200 UTC 16 February 2001 radiosonde sounding at Denver (located 50 km southeast of Boulder) is shown in Fig. 4. A deep temperature inversion extends from 400 to 900 AGL, high relative humidity exists below 500 m, and a tropopause height near 10 km are indicated in both the radiosonde and radiometer soundings. The retrieved fog/stratus water content maximum density of 0.14 g m^{-3} (inset in Fig. 4) located near 300 m AGL is consistent with observations of fog at this time (e.g., Gerber et al. 1999).

Poor visibility and icing conditions during this upslope event led to major disruptions in surface and air transportation in the Denver area, including diversion of flights from Denver International Airport for 18 hours. Fog was not predicted by numerical forecasts that used the Denver rawinsonde. However, in a retrospective study with the MM5 adjoint model, it was possible to reproduce the fog in the Boulder-Denver area through assimilation of the Boulder radiometric retrievals (Vandenberghe and Ware, 2003).

Eleven hours prior to the fog, the 0000 UTC 16 February Boulder radiometric retrieval (Fig. 2) and Denver radiosonde sounding (not shown) showed relative humidity less than 45% below 500 m height. During the following 11 h, the 5-min retrieved relative humidity increased somewhat prior to the rapid increase to >90% following the cold frontal passage at 1045 UTC. A similar trend was observed in Boulder prior to another similar event that produced supercooled

fog, freezing drizzle, and snow on 4 March 2003. Radiometric retrievals, weather radar, cloud radar, lidar and tower observations during this weather event are described in Herzegh et al. (2003) and Rasmussen and Ikeda (2003). The high-resolution radiometer measurements in both cases suggest that trends in relative humidity can be used to more accurately predict the onset of fog. Increased skill is expected if raw radiometric brightness temperatures (rather than retrieved profiles) are directly assimilated into numerical weather models (Nehrkorn et al. 2003).

b. Snowfall

Radiometric retrievals during a light snowfall event in Boulder on 23 December 2002 are shown over the lowest 3 km AGL in Fig. 5. Relatively dry snow that sublimated several minutes after touching the ground was visually observed at the radiometer site. Temperature profiles up to 3 km AGL (Fig. 5a) are less than 270 K and show a gradual warming below 500 m AGL from 1600 to 2100 UTC, followed by a cooling trend. Relative humidity (with respect to water, Fig. 5b) exceeds 90% between 0.5 and 2 km AGL during most of the observation period. “Equivalent” liquid density of about 0.1 g m^{-3} magnitude is analyzed between 0.5 and 1.2 km AGL from 2050 to 2210 UTC in Fig. 5c. The liquid water density retrieval is termed “equivalent” because the physical retrieval model is based on liquid emission only and does not include emission or scattering from snow or rain. Dry snow would be expected to produce a very small positive bias. If ice (and rain) emission and scattering are included in the retrieval model, and higher-frequency channels (e.g., 90 GHz) are included, then liquid and ice retrievals can be obtained (Li et al. 1997).

Figures 5e, 6b, and 6d indicate a continuous cloud layer with a cloud base temperature (T_{IR}) of 264 K over the radiometer during the 19-23 UTC interval. During this period the surface temperature was around 271 K, the integrated water vapor fluctuated around 6.6 mm, and the

integrated cloud water exhibited peak values that oscillated between 0.14 and 0.34 mm between 2030 and 2215. The snow that formed during this period would have likely exhibited some riming within this layer of supercooled water.

The Denver (DEN) radiosonde sounding at 0000 UTC on 24 December 2002 and the Boulder radiometer sounding at 2354 UTC on 23 December 2002 are shown in Fig. 7. The radiometric temperature retrieval is 2-3 K warmer than the radiosonde sounding from 1 to 3 km AGL, and is ~8 K warmer at the tropopause. The radiosonde relative humidity measurement increases from 65% at the surface to 80% at 700 m height and then remains above 75% up to 4.5 km height. The retrieved radiometer relative humidity increases from 80% at the surface to near saturation at 0.9 km (close to the cloud base temperature of 264 K) and remains close saturation to 1.75 km. These temperature and humidity differences between DEN and the radiometer may be attributed to sampling differences (Lagrangian point sampling for the radiosonde and fixed volume measurements for the radiometer), to the vertical resolution characteristics of the instruments, and to atmospheric variability over the 50 km distance between the two measurement locations.

During the 11 hours prior to snowfall, relative humidity at 1 km AGL steadily increased from 50% to 100%. Since saturation is required for cloud and precipitation formation, relative humidity profile trends could potentially improve local short-term cloud and precipitation forecasting.

c. Bores and gravity wave phenomena

Bores and gravity wave phenomena are relatively common, but their detailed thermodynamic structure has been difficult to measure because of their relatively short period and wavelength. Bores are hydraulic jumps that are often triggered by a density current (gust front) or

cold front intruding into a stable air mass near the surface (Simpson 1997). They are typically associated with a low-level wind shift in the direction of bore motion and a permanent upward displacement of the low-level air mass. A recent study by Knupp (2006) utilized the MPR (with only 14 min temporal resolution) and other MIPS instruments to examine a bore passage in Oklahoma. In this section, one-minute measurements of a “typical” bore are presented to illustrate the thermodynamic properties of bores at much higher temporal resolution.

On 16 May 2007 a well-formed bore was sampled around 0500 UTC (2330 LST) in advance of a weakening mesoscale convective system (MCS). During the bore passage, the surface temperature decreased by 2 - 3 °C, and the dewpoint increased more slowly by about the same magnitude (Fig. 8a). A distinct wind shift from 200° to 250° was recorded from the surface (Fig. 8b) up to about 0.8 km AGL, and a relative maximum in surface wind (gust to 7 m s⁻¹, Fig. 8c) was followed by weak surface flow of <2 m s⁻¹. The absence of a feeder flow (as indicated by the surface wind speed decrease to 1-2 m s⁻¹ following the bore passage), plus the sustained increase in surface pressure of about 1 hPa (relative to the background trend indicated in Fig. 8d) are characteristic surface signatures of bores (e.g., Koch et al. 1991, Knupp 2006).

The MPR analysis in Fig. 9a,b shows a well-defined reduction in θ (i.e., a rise in the isentropes) over the lowest 1.2 km, and a significant increase in r_v over a deeper layer due to the upward displacement of air within the bore, and horizontal advection following the bore, at low levels. The hydrostatic pressure increase associated with the observed average cooling of about 2 K over the lowest 1200 m is about 0.9 hPa, which duplicates the measured surface pressure increase during the bore passage.

Data from the 915 MHz wind profiler (not shown) indicated an updraft of 1-2 m s⁻¹ over the lowest 1.5 km. The 915 MHz SNR patterns suggest that a cumulus cloud extended to 3.8 km

AGL within the summit of this updraft located above the bore front. The ceilometer (Fig. 9c) recorded a cloud base near 1.5 km AGL within this updraft, and clouds persisted near 1.7 km AGL level following the bore passage. Indeed, the MPR integrated liquid value of 1.6 mm (Fig. 8g) is consistent with a cloud of 2.3 km depth, as suggested by the 915 MHz SNR (not shown).

Since both θ and r_v are conserved (for subsaturated adiabatic motion), the upward displacements of the isentropes and isohumes provide an estimate of the upward displacement distance of air parcels in this case. The 299 K isentrope (highlighted dashed line in Fig. 7a) ascended 0.8 km, while the 9 g kg^{-1} isohume rose about 0.9 km. The enhanced aerosol backscatter within the residual layer (Fig. 9c) shows a rise that is nearly simultaneous with that of the θ and r_v contours. While the isentropes assumed a horizontal orientation following the initial bore passage, the isohumes exhibit an undulation in time. This latter pattern suggests that waves were present in the wake of the bore, an observation that suggests this was an undular bore (Clarke et al. 1981). The moistening of the lower atmosphere associated with the bore passage was significant in this case, as values of integrated water vapor (IWV) increased by about 6 mm, or 20% (Fig. 8g). Moreover, the lifting associated with the bore destabilized the lowest 0.4 km, based on analysis of Brunt-Vaisala frequency computed from retrieved MPR temperature profiles.

d. Fine-scale structure of a cold front

MPR observations of cold fronts, gust fronts, and other boundaries often disclose fine-scale structures that have enhanced understanding of these types of phenomena. For example, Karan and Knupp (2006) described profiler observations (collected during the International H₂O Project, IHOP) of several boundary types.

On 16 March 2007 a relatively strong and complex cold front was sampled by the MIPS. Figure 10 shows the MPR θ and r_v retrievals along with the 915 MHz SNR around the time of the

frontal passage. Corresponding surface time series are presented in Fig. 11. A total of five thermodynamic transitions (labeled 1-5 in Figs. 10 and 11) are identified by the vertical dashed lines. The first boundary, associated with rainfall evaporation near the leading edge of the frontal rainband identified in Fig. 11c, is marked by surface cooling of ~ 2 K, and a surface wind shift to 4 m s^{-1} northerly flow below 0.5 km AGL. This feature resembles a shallow density current, a common feature of squall lines.

More appreciable cooling and drying was associated with the surface passage of the cold front, identified as the vertical dashed line labeled 2. This frontal feature was marked by an increase in northerly winds to 6 m s^{-1} (10 m s^{-1} aloft), a second distinct temperature break at the surface, and a modest pressure increase of 1 hPa (Figs. 11a,b). While the MPR indicates that cooling was most substantial below 1 km AGL, cooling did extend to 3-4 km AGL, and is corroborated by the lowering of the bright-band level shown in Fig. 10c.

A second cold frontal gradient (labeled 3) that passed overhead near 0840 UTC is most evident in (i) the r_v field above 0.6 km AGL (Fig. 10b), (ii) the θ field (a secondary cold surge) between 0.5 and 1.5 km AGL (Fig. 10a), and (iii) a significant reduction in IWV (Fig. 11f). This feature was associated with enhanced 915 MHz backscatter, which is inferred to represent enhanced Bragg scattering from mixing within this frontal zone. Normally, such a signature indicates the presence of cloud, but in this case the lack of integrated cloud water (ICW) suggests that appreciable clouds were absent within the 1-3 km AGL layer. The slope of this SNR feature is consistent with the slope of the enhanced gradient in the r_v field. At the surface, the only significant surface feature was a 1.5 mb pressure increase; changes in thermodynamic variables were insignificant.

A third frontal gradient (labeled as 4) is represented by significant cold advection beginning near 1040 UTC between 0.5 and 4.0 km AGL. Again, the surface thermodynamic signature is very subtle, but a significant and sustained pressure rise marked the onset of this deep layer of cold advection aloft. Such a pressure increase is more typically associated with arrival of cold air at the surface.

The fourth and final frontal gradient (labeled 5) occurred just after 1500 UTC and is represented by the onset of advection of drier air and a secondary surge of cold air above 1.0 km AGL. The corresponding surface signatures include a modest drop in T_d and a secondary pressure surge.

During passage of the four cold frontal segments, the low-level atmosphere remained close to saturation, and hence the stratocumulus cloud base, as measured by the ceilometer (not shown), remained near 100-200 m AGL during the 0400-1400 UTC time period. However T_{IR} measurements (Fig. 11d) display a slow decrease that is commensurate with the decrease in surface T and T_d . The time series of integrated liquid water in Fig. 11f reveals the prefrontal rainband passage between 0500 and 0600, two shallow postfrontal showers near 0700, and a shallow drizzle shower (~ 1 km deep, as indicated by the 915 MHz profiler and annotated in Fig. 10c) that corresponds to the relative maximum in ICW near 1300 UTC.

A comparison of the post-frontal MPR sounding with the RSA radiosonde (located 14 km to the south) at 1117 and 1141 UTC, respectively is displayed in Fig. 12. The MPR sounding is 1500 s earlier than the RSA balloon sounding to account for temperature advection based on the observed 10 m s^{-1} northerly post-frontal wind. Cloud base and top are located near 985 and 900 hPa, respectively. Although the MPR did not fully resolve the sharp frontal temperature inversion near 880 hPa (about 2 km AGL) and the warm air between 870 and 680 hPa, the relative trend is

approximately retrieved. In this case, utilization of the 915 MHz profiler, which measured a relative maximum in SNR within the inversion layer near 1 km AGL, indicated by the dashed line in Figs. 10a,c, could have improved the MPR retrievals using techniques outlined in Gossard et al. (1999), Bianco et al. (2005), and Klaus et al (2006).

This cold front exhibited a complex structure consisting of four (five including the initial density current produced by rainfall evaporation) concentrated gradients in θ and/or r_v that were detected by the MPR. The surface thermodynamic and wind measurements sampled only the density current and initial cold frontal boundary. This case demonstrates that the MPR is an ideal instrument to study the characteristics of fronts – in particular elevated fronts or secondary frontal transition zones (e.g., cold fronts aloft; see Koch 2001, Locatelli et al. 2002, Schultz 2005). Such fine-scale frontal structures have not been well-resolved in previous studies.

e. *Rapid water vapor variations preceding deep convection*

The Huntsville MPR observations commonly reveal rapidly-changing water vapor profiles around deep convection, mesoscale convective systems and squall lines. MPR and surface observations of a relatively intense squall line on 8 June 2007 are shown in Figs. 13 and 14. The passage of the squall line near 2100 UTC was accompanied by a wind gust (10 m AGL) to 16 m s^{-1} (not shown), a surface temperature reduction of $11 \text{ }^\circ\text{C}$, a peak rainfall rate of 150 mm hr^{-1} , and a large pressure oscillation between the mesohigh within the convective region and a mesolow located within the trailing anvil region.

This case illustrates modest water vapor variability preceding the squall line, and also presents measurements on the thermodynamics of the squall line density current (cold pool), followed by a warm “wake low” sometimes observed at the rear of squall lines (Johnson 2001). We focus on the variability in water vapor for a 24 h period from 0600 UTC 8 June to 0600 UTC

9 June 2007. The step increase in water vapor mixing ratio (Fig. 13b) over the lowest 2 km around 0900 UTC is commonly associated with atmospheric bores (Section 3c), which appears to be the case here. The passage of a more prominent bore six hours earlier at 0300 UTC produced a similar enhancement in r_v . Following the enhancement in r_v at 0900 UTC, the water vapor field remained relatively steady until rapid fluctuations associated with weak showers (about 5 km deep) were recorded near 1740 UTC. Variations in θ and r_v coincide with a surface pressure fluctuation (Fig. 12b), which suggests this feature was a gravity wave. A second increase in r_v was recorded after 0300 UTC on 9 June, well after the squall line passage.

A relative minimum in low-level water vapor during the 1800-2000 UTC period preceded a significant increase immediately in advance of the squall line, whose gust front and convective core were sampled near 2100 UTC. Two MPR soundings at 2002 and 2032 (Fig. 15) reveal an appreciable increase in low-level r_v values that raised the mixed-layer CAPE (surface to 10 km AGL) from 1200 to 1700 J kg⁻¹ (a 42% increase), just before the arrival of the gust front at 2035 UTC.

The gust front and trailing density current annotated in Fig. 13a were well sampled by the MPR. The top of the cold air, approximated by bold 301 K isentrope, exhibits a variable height (less than 1 km AGL) following the initial gust front passage at 2045 UTC (see also Fig. 14a). Figures 13a and 13b show a high amplitude wave in both the θ and r_v contours. Prolonged downward motion (ice terminal fall speed plus subsidence) of 1-2 m s⁻¹ was measured between 2200 and 2300 by the 915 MHz wind profiler. The surface pressure variation (Fig. 14b) during this wave cycle exhibited a 2 h period and a total variation of 4.5 hPa from the maximum pressure at 2120 to the minimum pressure at 2300 UTC. This low pressure is hydrostatically consistent with the presence of warm air aloft. A comparison of MPR soundings at 2032 and

2302 (not shown) indicates that warming of 1-3 C and drying (r_v deficit of -4 g kg^{-1}) between 930 and 600 hPa accompanied the subsidence. Although wake lows have been observed frequently at the rear of squall lines with surface data (Loehrer and Johnson 1995) and have been reproduced with a linear model (e.g., Haertel and Johnson 2000), the MPR observations shown here represent their thermodynamic structure in far greater temporal detail than derived from balloon soundings in previous studies.

4. Discussion

Radiometric profiling provides temperature and humidity soundings with an accuracy equivalent to radiosondes for numerical weather modeling applications. In addition, the MPR provides information on the cloud liquid burden. Case studies of radiometric retrievals were presented on a supercooled fog produced by upslope flow, a snowfall, a bore, a complex cold front, and a squall line and its near environment. The case studies demonstrate the diverse measurement capability of profiling radiometers, and the abundance of new insights into physical processes of mesoscale phenomena that are afforded by the fine temporal resolution. These preliminary results demonstrate that radiometric methods for continuous thermodynamic profiling have significant potential for a variety of applications in atmospheric research and weather forecasting, as indicated in the following.

a. Research applications

The MPR provides very high temporal resolution thermodynamic profiles that greatly facilitate understanding of a wide variety of mesoscale, cloud, and boundary layer processes. The examples presented in section 3 reveal that MPR data, combined with data from other instruments such as UHF profilers, acoustic profilers and lidars, offer considerable scientific insight into rapidly varying, complex mesoscale phenomena.

1) BOUNDARIES

Sections 3c and 3d establish that the MPR can provide considerable detail on the rapidly-evolving thermodynamic structure of boundaries such as cold fronts, gust fronts, gravity waves, bores and other related phenomena. The passage of boundaries is associated with thermodynamic changes that occur on very short time scales of $O(1 \text{ min})$, far too short to be sampled by in situ radiosondes. The dynamics of these systems are highly dependent on the thermodynamic state of the ambient environment and, in the case of gravity currents, the thermodynamic characteristics of the dense fluid. The Froude number is defined as

$$F_r = C_{gc} / (gh\Delta\theta_v/\theta_{v0})^{1/2},$$

where C_{gc} is the observed density current propagation speed, h is the cold pool depth, $\Delta\theta_v$ is the virtual potential temperature deficit within the cold pool, θ_{v0} is the ambient virtual potential temperature, and g is the gravitational acceleration. F_r is an important parameter in the analysis of gravity current propagation speeds. Karan (2007) used thermodynamic profiles from the MPR, and combined them with radar measurements (which measure the gust front propagation speed C_{gc}) to determine F_r for a large and diverse sample of gust fronts.

MPR observations around boundaries reveal that water vapor is often enhanced within the updraft zone of boundaries, due to upward advection within updrafts (Karan 2007). Sustained upward motion therefore can prime the upper convective boundary layer and the overlying free atmosphere for convective initiation. The presence of upward bulges in water vapor during active CBL conditions is often correlated with thermal or boundary layer roll updrafts as well.

2) THERMODYNAMICS WITHIN CLOUD SYSTEMS

The MPR has potential for profiling the temperature, and hence buoyancy, within cloud systems, provided that retrievals are based on more sophisticated radiative transfer physics to account for scattering and emission by precipitation-sized water and ice. The gravity current illustrated in Fig. 13 is defined quite well because precipitation contamination is less significant at low levels within light to moderate rainfall rates⁵. Currently, no other ground-based remote sensing technique is able to routinely probe the temperature within (precipitating) cloud systems up to middle tropospheric levels. May et al. (2003) recently reported that radio acoustic sounding system (RASS) measurements with a 50 MHz profiler did not successfully retrieve virtual temperature within relatively vigorous convective systems due the apparent turbulent break-up of acoustic wave fronts. A more robust passive microwave retrieval scheme could, in principle, utilize information from profiling radars that sample reflectivity factor or Doppler spectra of the precipitation medium. Precipitation size distributions and particle types can then be retrieved from Doppler spectra (Williams et al. 2007), which could provide input to the radiative transfer model.

3) BOUNDARY LAYER PROCESSES

Because the MPR can continuously monitor the atmospheric boundary layer (ABL), rapid changes in nocturnal boundary layer (NBL) phenomena (e.g., gravity waves, bores; see Knupp 2006) can be monitored. NBL thermodynamic structures often exhibit very large vertical gradients in θ and r_v near the surface. Since the MPR resolution scales with height, such large gradients are often resolved quite well. Fig. 16 shows a comparison between the MPR and

Redstone Arsenal (RSA) soundings for a strong nocturnal inversion in Huntsville. The temperature profile within the surface-based nocturnal inversion is duplicated quite well.

The NBL and other statically stable layers are conducive to gravity wave propagation. The MPR combined with a 915 MHz profiler is able to resolve the presence of gravity waves in vertical motion, potential temperature and/or humidity fluctuations, as well as the environment (e.g., Scorer parameter which depends on vertical profiles of static stability and wind shear) that supports ducted gravity waves.

Rapid water vapor variations have not been resolvable by serial soundings in previous experimental programs. Such rapid variations are associated with large BL eddies, boundaries, and rapid horizontal advection. Since convective initiation (CI) is highly sensitive to relatively subtle changes in low-level r_v (Crook 1996, Weckwerth 2000), the MPR shows considerable potential in improving quantitative precipitation forecasting (QPF) when radiometer data are assimilated into models.

4) SEVERE STORMS AND THEIR ENVIRONMENT

Static stability, usually expressed in bulk form as the convective available potential energy (CAPE), is an important parameter in assessing severe storm potential. Likewise, analysis of convective inhibition (CIN, Colby 1984) is used to anticipate the timing of convective initiation. Rapidly changing vertical thermodynamic profiles are often produced locally through boundary layer heating, mesoscale vertical motion, and horizontal temperature advection. Continuous monitoring of thermodynamic indices can therefore provide very timely information on CAPE and CIN (e.g., Fig. 15). This capability has been demonstrated by Feltz and Mecikalski (2002), who utilized the hyper spectral Atmospheric Emitted Radiance Interferometer (AERI) instrument to assess the evolution of CAPE and CIN during the 3 May 1999 tornado outbreak in Oklahoma.

The MPR has been used by UAH researchers to determine the propagation modes of squall lines. Three different propagation modes have been identified, including the common density current mode (cold pool) which is very basic to squall line propagation and evolution (Bryan et al. 2006). In addition, the MPR has documented cases in which the squall line propagates as a bore and as a high-amplitude low-level ducted gravity wave. The latter has been considered previously in the form of a wave-CISK mechanism over the troposphere (Raymond 1984). The role of the cold pool in the bore and gravity wave cases is not apparent, and may play a more minor role than in squall lines associated with density currents.

b. Forecasting applications

Forecasting applications are many in number; some are directly connected to topics discussed in the previous section. As stated previously, an obvious application is assimilation of MPR thermodynamic profiles and integrated liquid water (or radiances) into mesoscale models.

1) QUANTITATIVE PRECIPITATION FORECASTING (QPF)

QPF is at the top of this list because of the recognized need to assimilate water vapor fields into mesoscale forecast models, in order to improve accuracy of QPF. This was a fundamental premise of the IHOP project (Weckwerth and Parsons 2006). As noted in Section 3a2, convective initiation in mesoscale models is very sensitive to relatively small three-dimensional variations in temperature and mixing ratio (Ducroq et al 2000). Initial numerical modeling based on IHOP data sets has demonstrated that assimilation of detailed 3-D water vapor fields produces a significant improvement in the model precipitation forecasts (Wulfmeyer et al. 2006).

2) AVIATION FORECASTING

The ability to detect supercooled liquid, as illustrated in Section 3a, is an obvious application of MPR measurements to aviation forecasting. This capability would make a potentially important contribution to the “current icing potential” (CIP, Bernstein et al 2005) which utilizes multiple data sources (e.g., surface, radar, satellite, PIREPs, forecast models, etc.).

3) WINTER WEATHER FORECASTING

MPR measurements have also been useful in winter precipitation forecasting, such as utilization of the lower atmospheric temperature/humidity profile to determine the relative probability of rain, freezing rain, and snow. This capability was used to explain an unexpected (but significant) sleet event around Huntsville, in which the entire lower atmosphere was just above 0 °C, but dry conditions promoted a low wet-bulb temperature ($T_w < 0$ °C), and hence cooling of raindrops and the initiation of raindrop freezing. Thus, profiles of T_w represent another useful application for real-time monitoring of winter weather.

Integrated measures of temperature, such as thickness, are extensively utilized to forecast winter precipitation type (e.g., Heppner, 1992). Radiometric measurements can be used quite effectively to monitor various thickness values (1000-925 hPa, 1000-850 hPa) since the integrated temperature measurement errors are likely less than point temperature errors.

4) SEVERE STORMS FORECASTING

Forecasting applications for the severe storms environment have been alluded to in previous sections. The MPR, used in conjunction with other profiling instruments such as UHF profiling radars, can provide continuous monitoring of CAPE (e.g., Feltz and Mecikalski 2002,

Feltz et al. 2003), wind shear, and parameters derived from combinations of thermodynamic and/or wind profiles such as storm-relative helicity and energy-helicity index (EHI) that are important ingredients in severe storms forecasts (Johns and Doswell 1992, Moller 2001).

5. Summary

The MPR offers a diverse set of measurements that potentially yield numerous benefits to both researchers and forecasters. Temperature and humidity profiles, along with integrated values of water vapor, cloud water, and even temperature in the form of thickness (acquired at 1-5 minute intervals in this study), represent the primary MPR measurements. This high temporal resolution provides the thermodynamic measurements needed to resolve the fine-scale structure of gravity waves, gust fronts, bores, cold fronts, and other boundaries. In addition, with improved retrieval techniques, the internal temperature (and hence buoyancy) of cloud systems can be determined. Assimilation of MPR data into mesoscale models shows considerable potential to substantially improve prediction of cloud/mesoscale processes, convective initiation, and precipitation. In this vein, a network of MPRs and co-located wind profilers (a mix of 915 MHz and 449 MHz systems) would very likely improve forecasts of high impact weather, precipitation, and a variety of other mesoscale phenomena.

Acknowledgements

Two of the authors (KRK and TAC) acknowledge support from the National Science Foundation under grants ATM-0079829 (used to procure the UAH MPR in 2001) and ATM-0533596. Dustin Phillips assisted in production of the figures.

Support from U.S. Army Research Laboratory contract DAAD17-01-C-0045 (E. Measure, Program Manager) is gratefully acknowledged.

References

- Bernstein, B.C., F. McDonough, M.K. Politovich, B.G. Brown, T.P. Ratvasky, D.R. Miller, C.A. Wolff, and G. Cuning, 2005: Current Icing Potential: Algorithm Description and Comparison with Aircraft Observations. *J. Appl. Meteor.*, **44**, 969–986.
- Bianco, L., D. Cimini, F.S. Marzano, and R. Ware, 2005: Combining microwave radiometer and wind profiler radar measurements for high-resolution atmospheric humidity profiling. *J. Atmos. Oceanic Technol.*, **22**, 949–965.
- Bryan, G.H., J.C. Knievel, and M.D. Parker, 2006: A multimodel assessment of RKW theory's relevance to squall-line characteristics. *Mon. Wea. Rev.*, **134**, 2772–2792.
- Chahine, M.T., T.S. Pagano, H.H. Aumann, R. Atlas, C. Barnet, J. Blaisdell, L. Chen, M. Divakarla, E.J. Fetzer, M. Goldberg, C. Gautier, S. Granger, S. Hannon, F.W. Irion, R. Kakar, E. Kalnay, B.H. Lambrigtsen, S.Y. Lee, J. Le Marshall, W.W. McMillan, L. McMillin, E.T. Olsen, H. Revercomb, P. Rosenkranz, W.L. Smith, D. Staelin, L.L. Strow, J. Susskind, D. Tobin, W. Wolf, and L. Zhou, 2006: AIRS: Improving weather forecasting and providing new data on greenhouse gases. *Bull. Amer. Meteor. Soc.*, **87**, 911–926.
- Clarke, R., R. Smith, and D. Reid, 1981: The Morning Glory of the Gulf of Carpentaria: An atmospheric undular bore. *Mon. Wea. Rev.*, **109**, 1726–1750.
- Colby, F.P., 1984: Convective inhibition as a predictor of convection during AVE-SESAME II. *Mon. Wea. Rev.*, **112**, 2239–2252.
- Crook, N.A., 1996: Sensitivity of moist convection forced by boundary layer processes to low-level thermodynamic fields. *Mon. Wea. Rev.*, **124**, 1767–1785

- Ducroqc, V., D. Ricard, J.-P. Lafore, and F. Orain, 2000: Storm-scale numerical rainfall prediction for five precipitating events over France: On the importance of the initial humidity field. *Weather and Forecasting*, **17**, 1236-1256.
- Feltz, W.F., and J.R. Mecikalski, 2002: Monitoring high-temporal-resolution convective stability indices using the ground-based Atmospheric Emitted Radiance Interferometer (AERI) during the 3 May 1999 Oklahoma–Kansas tornado outbreak. *Wea. Forecasting*, **17**, 445–455.
- Feltz, W.F., W.L. Smith, H.B. Howell, R.O. Knuteson, H. Woolf, and H.E. Revercomb, 2003: Near-continuous profiling of temperature, moisture, and atmospheric stability using the Atmospheric Emitted Radiance Interferometer (AERI). *J. Appl. Meteor.*, **42**, 584–597.
- Gerber, H., G. Frick, and A.R. Rodi, 1999: Ground-based FSSP and PVM measurements of liquid water content. *J. Atmos. Ocean. Tech.*, **16**, 1143-1149.
- Gossard, E.E., S. Gutman, B. B. Stankov, and D. E. Wolf, 1999: Profiles of radio refractive index and humidity derived from radar wind profilers and the Global Position System. *Radio Sci.*, **34**, 371–383.
- Güldner, J., and D. Spänkuch, 2001: Remote sensing of the thermodynamic state of the atmospheric boundary layer by ground-based microwave radiometry. *J. Atmos. Ocean. Tech.*, **18**, 925-933.
- Haertel, P.T., and R.H. Johnson, 2000: The linear dynamics of squall line mesohighs and wake lows. *J. Atmos. Sci.*, **57**, 93–107.
- Heppner, P.O., 1992: Snow versus rain: Looking beyond the “magic” numbers. *Wea. Forecasting*, **7**, 683–691.

- Herzogh, P., S. Landolt, and T. Schneider, 2003: The structure, evolution and cloud processes of a Colorado upslope storm as shown by profiling radiometer, radar, and tower Data. *Proc. 31st Conf. on Radar Meteor.*, Seattle, WA, Amer. Met. Soc.
- Hogg, D., M. Decker, F. Guiraud, K. Earnshaw, D. Merritt, K. Moran, W. Sweezy, R. Strauch, E. Westwater, and G. Little, 1983: An automatic profiler of the temperature, wind and humidity in the troposphere, *J. Clim. Appl. Meteorol.*, **22**, 807-831.
- Johns, R.H., and C.A. Doswell, 1992: Severe local storms forecasting. *Wea. Forecasting*, **7**, 588–612.
- Johnson, R.H., 2001: Surface mesohighs and mesolows. *Bull. Amer. Meteor. Soc.*, **82**, 13–31.
- Karan, H., 2007: Thermodynamic and kinematic characteristics of low-level convergence zones observed by the Mobile Integrated Profiling System. Ph.D. dissertation, University of Alabama in Huntsville, 207 pp.
- Karan, H., and K. Knupp, 2006: Mobile Integrated Profiler System (MIPS) observations of low-level convergent boundaries during IHOP. *Mon. Wea. Rev.*, **134**, 92–112.
- Klaus, V., L. Bianco, C. Gaffard, M. Matabuena, and T. Hewison, 2006: Combining UHF radar wind profiler and microwave radiometer for the estimation of atmospheric humidity profiles. *Met. Zeit.*, **15**, 87-97.
- Knupp, K., 2006: Observational analysis of a gust front to bore to solitary wave transition within an evolving nocturnal boundary layer. *J. Atmos. Sci.*, **63**, 2016–2035.
- Koch, S.E., P.B. Dorian, R. Ferrare, S. Melfi, W.C. Skillman, and D. Whiteman, 1991: Structure of an internal bore and dissipating gravity current as revealed by Raman lidar. *Mon. Wea. Rev.*, **119**, 857–887.

- Koch S. E., 2001: Real-time detection of split fronts using mesoscale models and WSR-88D radar products. *Wea. Forecasting*, **16**, 35–55.
- Li, L., J. Vivekanandan, C. H. Chan, and L. Tsang, 1997: Microwave radiometric technique to retrieve vapor, liquid and ice. *IEEE Trans. Geosci. Rem. Sens.*, **35**, 224–236.
- Liljegren, J., E. Clothiaux, S. Kato, B. Lesht, F., 2001: Initial evaluation of profiles of temperature, water vapor and cloud liquid water from a new microwave profiling radiometer, *Proc. 5th Symp. Integrated Observing Systems*, Albuquerque, NM, Am. Met. Soc.
- Locatelli, J.D., R.D. Schwartz, M.T. Stoelinga, and P.V. Hobbs, 2002: Norwegian-type and cold front aloft-type cyclones east of the Rocky Mountains. *Wea. Forecasting*, **17**, 66–82.
- Loehrer, S. M., and R. H. Johnson, 1995: Surface pressure and precipitation life cycle characteristics of PRE-STORM mesoscale convective systems. *Mon. Wea. Rev.*, **123**, 600–621
- May, P.T., C. Lucas, R. Latatits, and I.M. Reid, 2003: On the use of 50-MHz RASS in thunderstorms. *J. Atmos. Oceanic Technol.*, **20**, 936–943.
- Nehrkorn, T., and C. Grassotti, 2003: Mesoscale variational assimilation of profiling radiometer data. *16th Conf. on Numerical Weather Prediction*, Seattle, WA, Amer. Met. Soc.
- Rasmussen, R., and K. Ikeda, 2003: Radar observations of a freezing drizzle case in Colorado, *31st Conf. on Radar Meteor.*, Seattle, WA, Amer. Met. Soc.
- Raymond, D.J., 1984: A Wave-CISK model of squall lines. *J. Atmos. Sci.*, **41**, 1946–1958.
- Schultz, D.M., 2005: A review of cold fronts with prefrontal troughs and wind shifts. *Mon. Wea. Rev.*, **133**, 2449–2472.
- Simpson, J. E., 1997: *Gravity Currents: In the Environment and the Laboratory*. Cambridge University Press, 244 pp.

- Solheim, F., J. Godwin, E. Westwater, Y. Han, S. Keihm, K. Marsh, R. Ware, 1998: Radiometric profiling of temperature, water vapor, and liquid water using various inversion methods, *Rad. Sci.*, **33**, 393-404.
- Stankov, B.B., E. E. Gossard, B. L. Weber, R. J. Latatits, A. B. White, D. E. Wolfe, and D. C. Welsh, 2003: Humidity gradient profiles from wind profiling radars using the NOAA/ETL advanced Signal Processing System (SPS). *J. Atmos. Oceanic Technol.*, **20**, 3–22.
- Vandenberghe, F., and R. Ware, 2003: 4-dimensional variational assimilation of ground-based microwave observations during a winter fog event, *International Workshop on GPS Meteorology*, Tsukuba, Japan.
- Ware, R., R. Carpenter, J. Guldner, J. Liljegren, T. Nehrkorn, F. Solheim, and F. Vandenberghe, 2003a: A multi-channel radiometric profiler of temperature, humidity and cloud liquid, *Rad. Sci.*, **38**, 8079-8032.
- Weckwerth, T. M., 2000: The effect of small-scale moisture variability on thunderstorm initiation. *Mon. Wea. Rev.*, **128**, 4017–4030.
- Weckwerth, T.M., and D.B. Parsons, 2006: A review of convection initiation and motivation for IHOP_2002. *Mon. Wea. Rev.*, **134**, 5–22.
- Westwater, E., 1993: Ground-based microwave remote sensing of meteorological variables. Chapter 4 in *Atmospheric Remote Sensing by Microwave Radiometry*, J. Wiley & Sons, Inc., M. Janssen (ed.), 145-213.
- Westwater, E., Y. Han, and F. Solheim, 2000: Resolution and accuracy of a multi-frequency scanning radiometer for temperature profiling, *Microw. Radiomet. Remote Sens. Earth's Surf. Atmosphere*, Pampaloni and Paloscia (ed.), VSP (publisher), The Netherlands, 129-135.

- Williams, C.R., A.B. White, K.S. Gage, and F.M. Ralph, 2007: Vertical structure of precipitation and related microphysics observed by NOAA profilers and TRMM during NAME 2004. *J. Climate*, **20**, 1693–1712.
- Wulfmeyer, V., H.S. Bauer, M. Grzeschik, A. Behrendt, F. Vandenberghe, E.V. Browell, S. Ismail, and R.A. Ferrare, 2006: Four-dimensional variational assimilation of water vapor differential absorption lidar data: The first case study within IHOP_2002. *Mon. Wea. Rev.*, **134**, 209–230.
- Zhou, D.K., W.L. Smith, X. Liu, A.M. Larar, S.A. Mango, and H.L. Huang, 2007: Physically retrieving cloud and thermodynamic parameters from ultraspectral IR measurements. *J. Atmos. Sci.*, **64**, 969–982.

Figure captions

Figure 1. Radiometric retrieval accuracy determined by all season comparison with radiosondes. Radiosonde errors are those typically assigned by the National Centers for Environmental Prediction when radiosonde data are used in numerical weather modeling. Statistics of radiometric retrieval comparisons with radiosonde soundings are taken from Gldner and Spnkuch (2001) and Liljegren, (2001).

Figure 2. Radiometric retrievals (plotted in time vs. height format) of (a) temperature, (b) relative humidity, and (c) liquid water density (drawn at 0.1 g m^{-3} intervals starting at 0.1 g m^{-3}) during a supercooled fog event associated with upslope flow at Boulder on 16 February 2001. The vertical dashed lines indicate the time of frontal passage and subsequent fog arrival over the radiometer.

Figure 3. Surface time series derived the radiometer: (a) temperature and relative humidity, (b) infrared temperature, (c) integrated water vapor, and (d) integrated cloud water for the same time period as in Fig. 2. The frontal passage and fog arrival are indicated by the vertical dashed lines.

Figure 4. Boulder retrieval (solid) and Denver radiosonde sounding (dashed), showing an inversion from the surface to 1 km AGL and low dew point depression (high relative humidity) up to 300 m AGL at 1200 UTC on 16 Feb 2001. The radiometric liquid water retrieval (inset, lower right, matched to the skew-T pressure levels) shows a maximum liquid water density of 0.14 g m^{-3} near 300 m AGL.

Figure 5. As in Fig. 2, except for 23 December 2002. Relative humidity is near saturation around 1 km AGL, and corresponds to low values “equivalent” liquid, drawn at 0.02 g m^{-3} intervals starting at 0.02 g m^{-3} .

Figure 6. As in Fig. 3, except for 23 December 2002. Vertical dashed lines mark the distinct cloud borders.

Figure 7. MPR retrieved sounding (black) and Denver radiosonde (gray) for a light snowfall event at Boulder on 23 Dec 2002. The MPR sounding shows relative humidity saturation from 1 to 2 km height and 0.07 g m^{-3} equivalent liquid density (inset, lower right, matched to the skew-T pressure levels) near 1 km height.

Figure 8. Time series of surface parameters (derived from independent surface instrumentation) and MPR data from the bore case of 16 May 2007. Surface parameters include (a) temperature and dewpoint temperature, (b) 10 m wind direction, (c) 10 m wind speed, and (d) pressure (reduced to sea-level). MPR parameters include (e) IR temperature, (f) integrated water vapor (or precipitable water), and (g) integrated cloud water. The vertical dashed line represents the bore passage.

Figure 9. Time vs. height sections of parameters illustrating the passage of a bore on 16 May 2007. (a) MPR-derived potential temperature, contoured every 2 K (the 299 K isentrope is dashed), (b) MPR-derived mixing ratio, contoured every 0.5 g kg^{-1} (the 9 g kg^{-1} isohume is dashed), and (c) range normalized ceilometer backscatter (black shading exceeds values on the scale to the right). The 299 K isentrope from panel a is drawn as the red dashed line in panel c. The vertical dashed line represents the bore passage.

Figure 10. Time vs. height sections of parameters illustrating the passage of a cold frontal system on 16 March 2007. (a) MPR-derived potential temperature, contoured every 2 K, (b) MPR-derived mixing ratio, contoured every 0.5 g kg^{-1} , and (c) 915 MHz backscatter expressed in a signal-to-noise ratio (dB). Vertical lines labeled 1-5 refer to frontal features that are defined in the text. The frontal inversion, inferred from the 915 MHz SNR, is shown as a dashed line in

panel c, and is overdrawn on the isentropes in panel a. The solid line in panel c represents the 0 °C isotherm from the MPR retrieval. The warm bias produced by precipitation scattering and emission is represented by the upward protrusion of the isotherm above the bright band in panel c (between dashed lines 1 and 2).

Figure 11. Time series of surface data (derived from independent surface instrumentation) and MPR data from the cold frontal system on 16 March 2007. Surface parameters include (a) temperature and dewpoint temperature, (b) pressure (reduced to sea-level), and (c) 10 m wind speed. MPR parameters include (d) IR temperature, (e) integrated water vapor (or precipitable water), and (f) integrated cloud water. The vertical dashed lines depict frontal gradients identified in Fig. 10.

Figure 12. MPR and RSA soundings (16 March 2007 cold front), plotted on a skew-T, ln p diagram.

Figure 13. Time vs. height sections of parameters illustrating the pre-storm environment and the passage of a squall line on 8 June 2007. (a) MPR-derived potential temperature, contoured every 2 K, (b) MPR-derived mixing ratio, contoured every 0.5 g kg⁻¹, (c) 915 MHz backscatter expressed in a signal-to-noise ratio (dB), and (d) 915 MHz radial velocity from the vertical beam. The warm bias produced by precipitation scattering and emission is present in panels a and b (between vertical lines), but the low-level potential temperature appears to have experienced much lower bias. The 301 K isotherm is bold in panel a to depict the low-level density current.

Figure 14. Time series of surface data (derived from independent surface instrumentation) and radiometer data from the 8 June 2007 squall line case. Surface parameters include (a) temperature and dewpoint temperature and (b) pressure (reduced to sea-level). MPR parameters

include (c) IR temperature, (d) integrated water vapor (or precipitable water), and (e) integrated cloud water. The vertical dashed lines refer to significant features that are annotated in panels a and b.

Figure 15. MPR soundings, plotted on a skew-T, ln p diagram. These soundings were sampled just in advance of the squall line and illustrate the rapid destabilization produced by an increase in low-level mixing ratio. Dashed lines represent saturated adiabats based on the lowest 50 mb average values of potential temperature and mixing ratio for each sounding.

Figure 16. Nocturnal inversion soundings from the MPR and Redstone Arsenal (RSA) radiosonde at 1202 UTC on 26 March 2007.

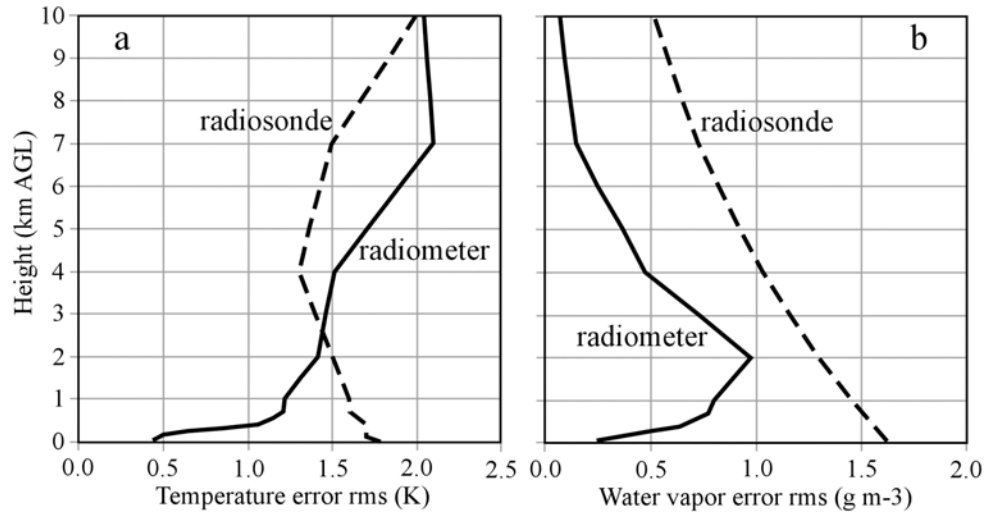


Figure 1. Radiometric retrieval accuracy determined by all season comparison with radiosondes. Radiosonde errors are those typically assigned by the National Centers for Environmental Prediction when radiosonde data are used in numerical weather modeling. Statistics of radiometric retrieval comparisons with radiosonde soundings are taken from Gldner and Spnkuch (2001) and Liljegren, (2001).

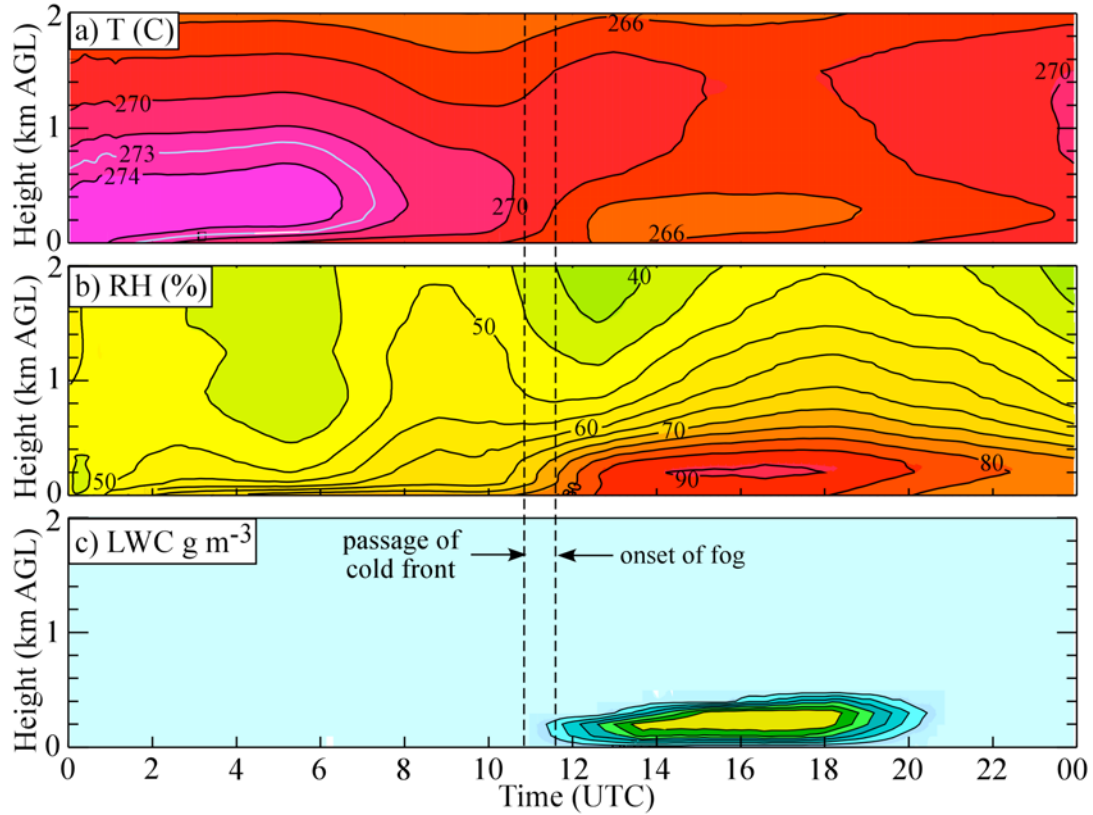


Figure 2. Radiometric retrievals (plotted in time vs. height format) of (a) temperature, (b) relative humidity, and (c) liquid water density (drawn at 0.1 g m^{-3} intervals starting at 0.1 g m^{-3}) during a supercooled fog event associated with upslope flow at Boulder on 16 February 2001. The vertical dashed lines indicate the time of frontal passage and subsequent fog arrival over the radiometer.

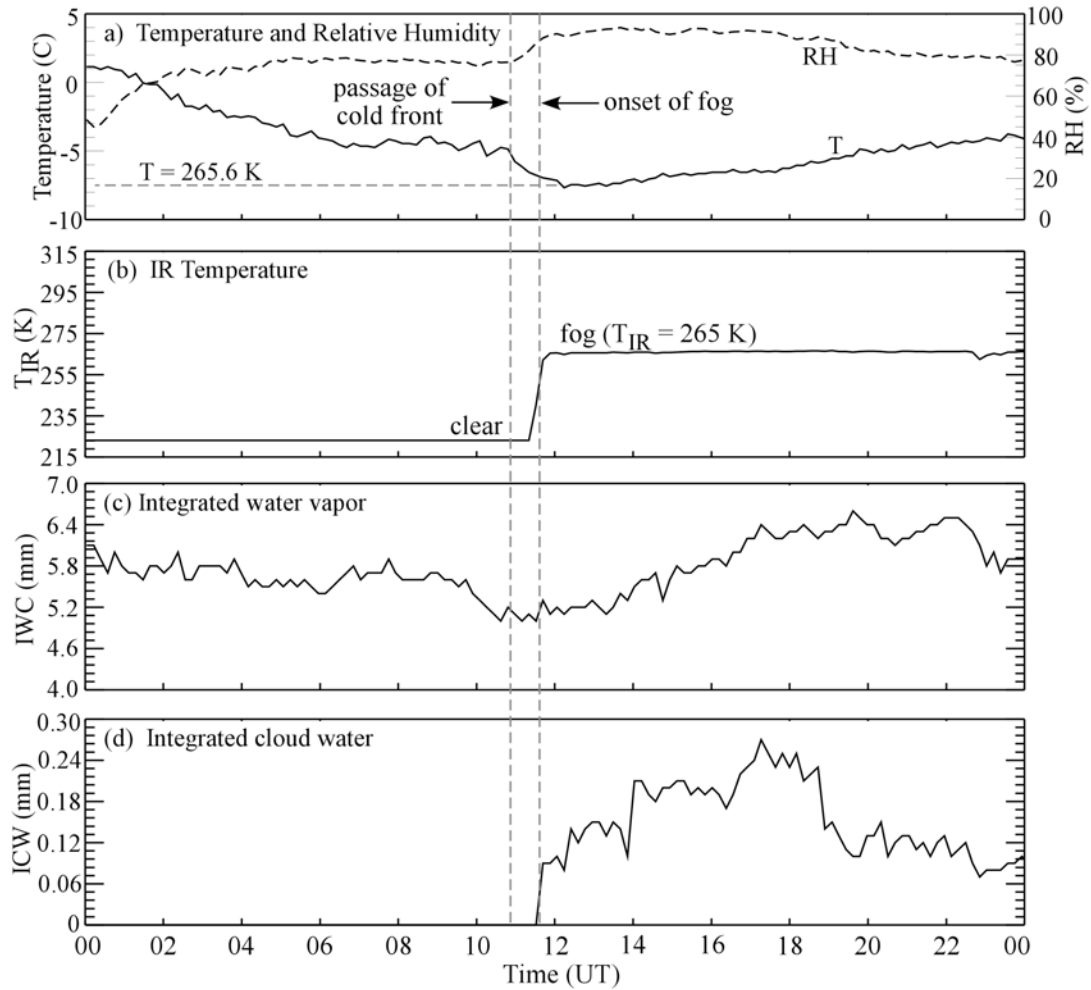


Figure 3. Surface time series derived the radiometer: (a) temperature and relative humidity, (b) infrared temperature, (c) integrated water vapor, and (d) integrated cloud water for the same time period as in Fig. 2. The frontal passage and fog arrival are indicated by the vertical dashed lines.

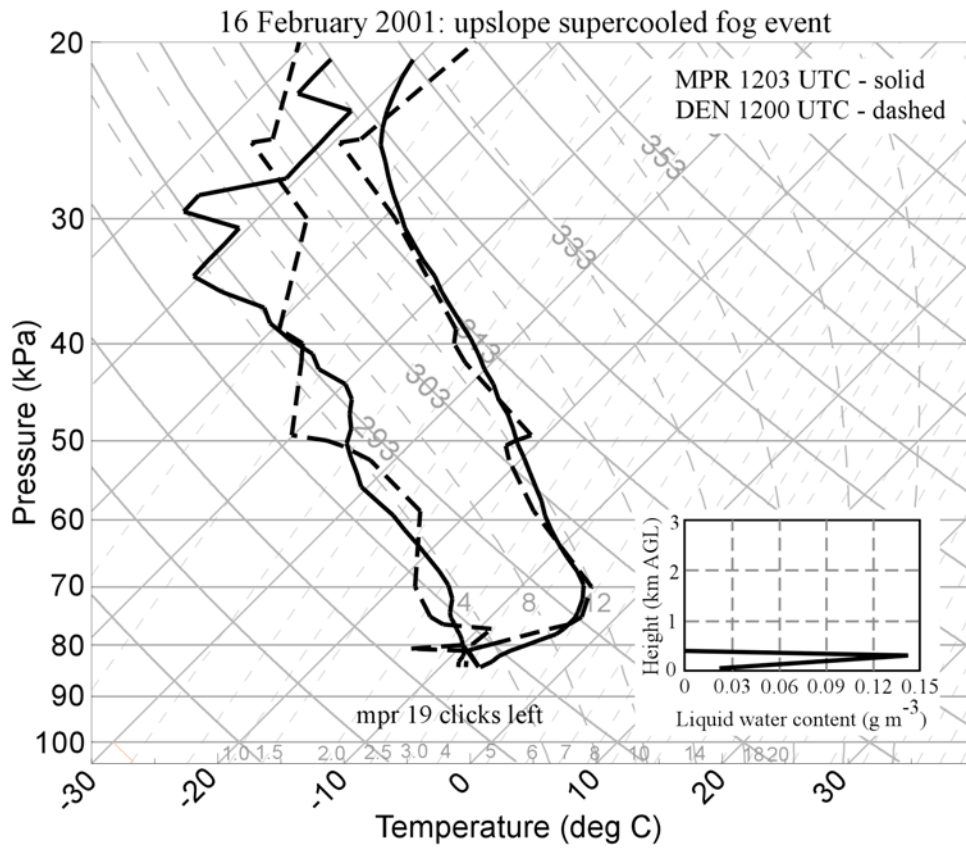


Figure 4. Boulder retrieval (solid) and Denver radiosonde sounding (dashed), showing an inversion from the surface to 1 km AGL and low dew point depression (high relative humidity) up to 300 m AGL at 1200 UTC on 16 Feb 2001. The radiometric liquid water retrieval (inset, lower right, matched to the skew-T pressure levels) shows a maximum liquid water density of 0.14 g m⁻³ near 300 m AGL.

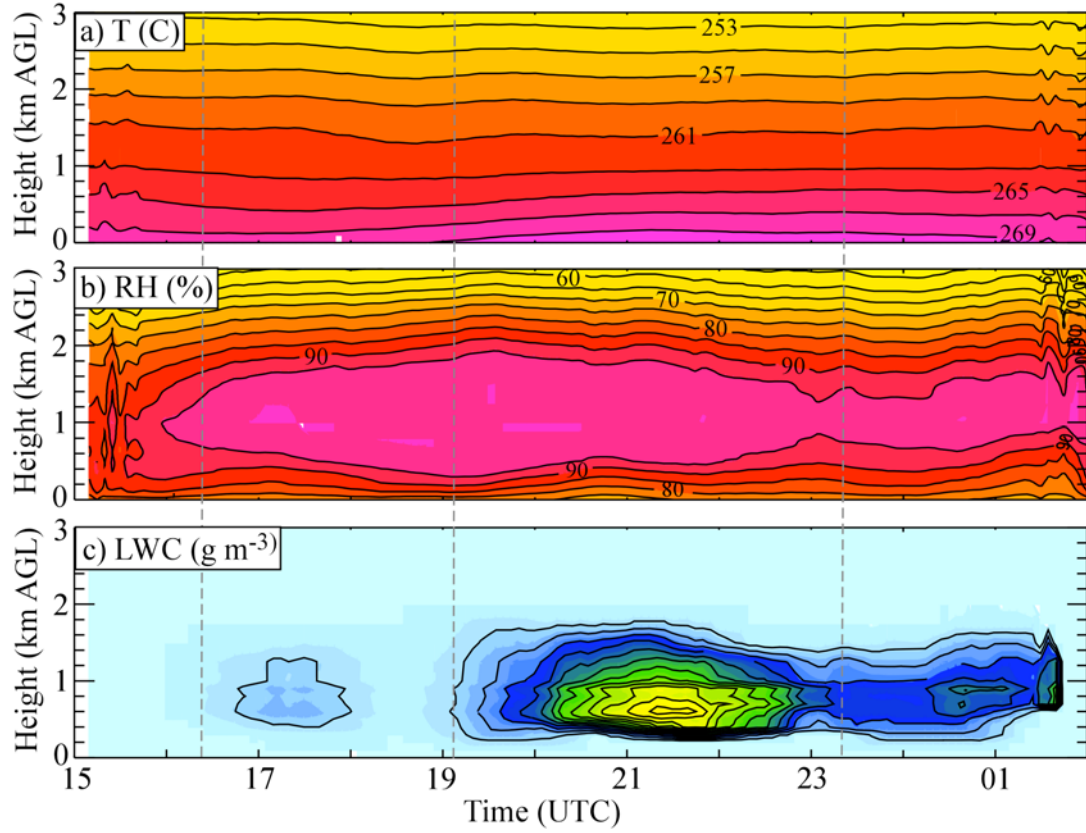


Figure 5. As in Fig. 2, except for 23 December 2002. Relative humidity is near saturation around 1 km AGL, and corresponds to low values “equivalent” liquid, drawn at 0.02 g m^{-3} intervals starting at 0.02 g m^{-3} .

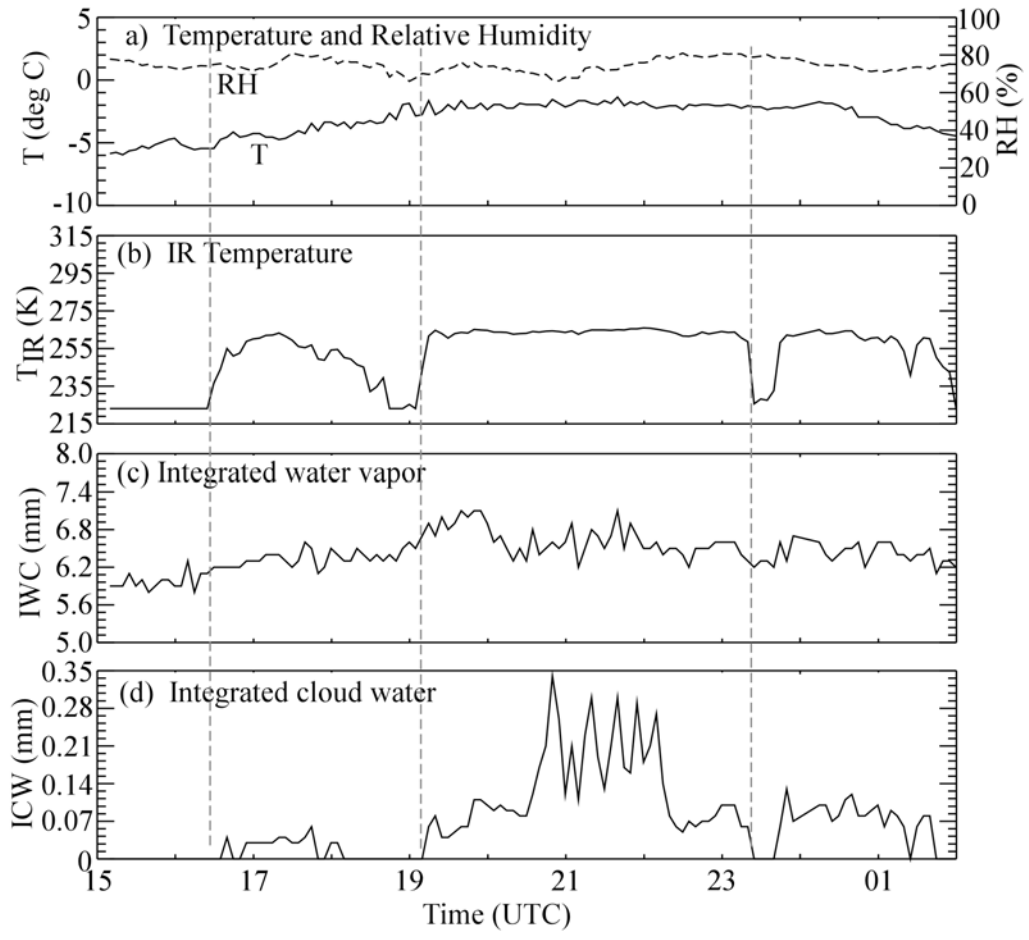


Figure 6. As in Fig. 3, except for 23 December 2002. Vertical dashed lines mark the distinct cloud borders.

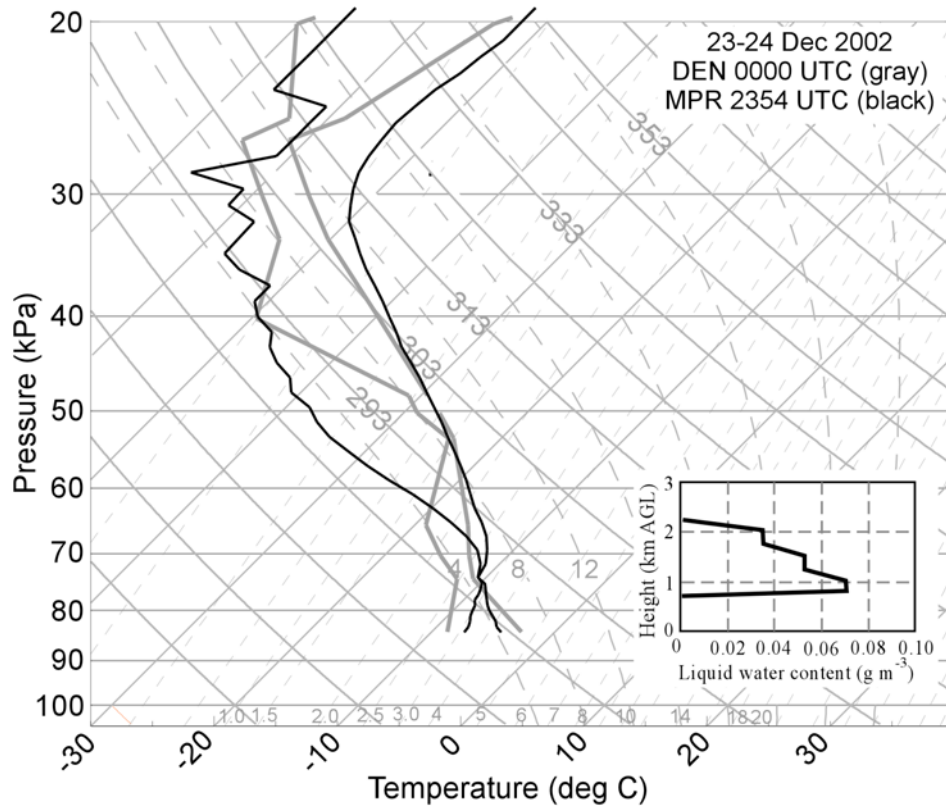


Figure 7. MPR retrieved sounding (black) and Denver radiosonde (gray) for a light snowfall event at Boulder on 23 Dec 2002. The MPR sounding shows relative humidity saturation from 1 to 2 km height and 0.07 g m^{-3} equivalent liquid density (inset, lower right, matched to the skew-T pressure levels) near 1 km height.

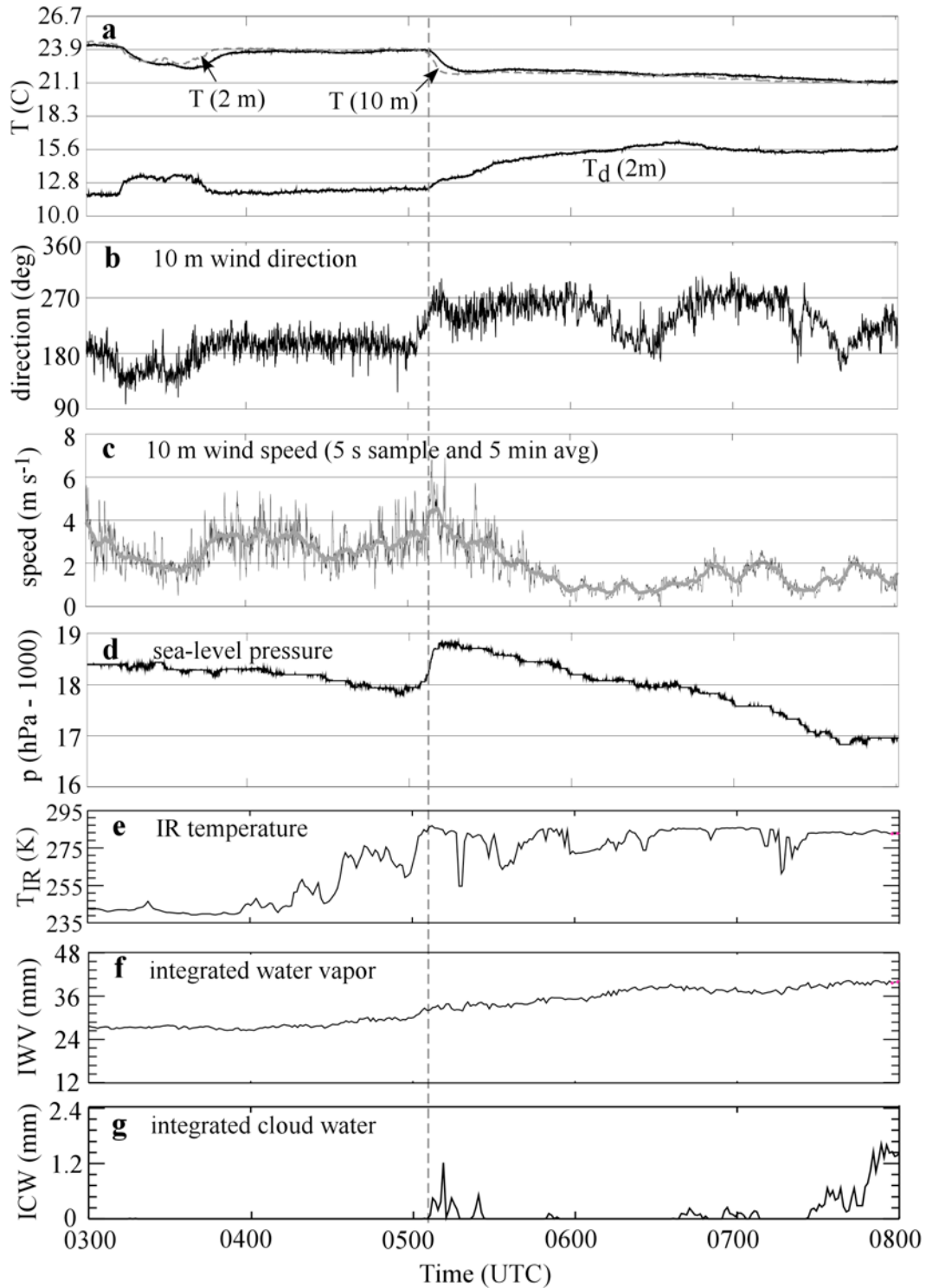


Figure 8. Time series of surface parameters (derived from independent surface instrumentation) and MPR data from the bore case of 16 May 2007. Surface parameters include (a) temperature and dewpoint temperature, (b) 10 m wind direction, (c) 10 m wind speed, and (d) pressure (reduced to sea-level). MPR parameters include (e) IR temperature, (f) integrated water vapor (or precipitable water), and (g) integrated cloud water. The vertical dashed line represents the bore passage.

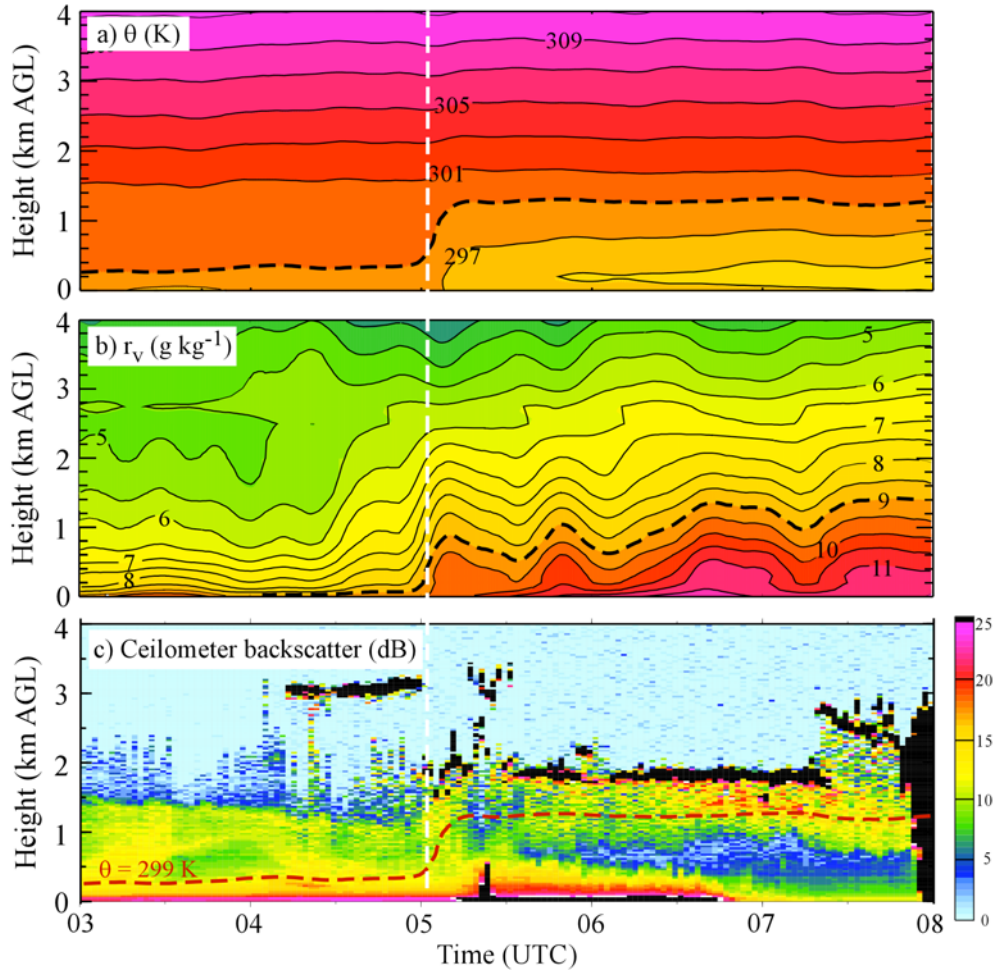


Figure 9. Time vs. height sections of parameters illustrating the passage of a bore on 16 May 2007. (a) MPR-derived potential temperature, contoured every 2 K (the 299 K isentrope is dashed), (b) MPR-derived mixing ratio, contoured every 0.5 g kg^{-1} (the 9 g kg^{-1} isohume is dashed), and (c) range normalized ceilometer backscatter (black shading exceeds values on the scale to the right). The 299 K isentrope from panel a is drawn as the red dashed line in panel c. The vertical dashed line represents the bore passage.

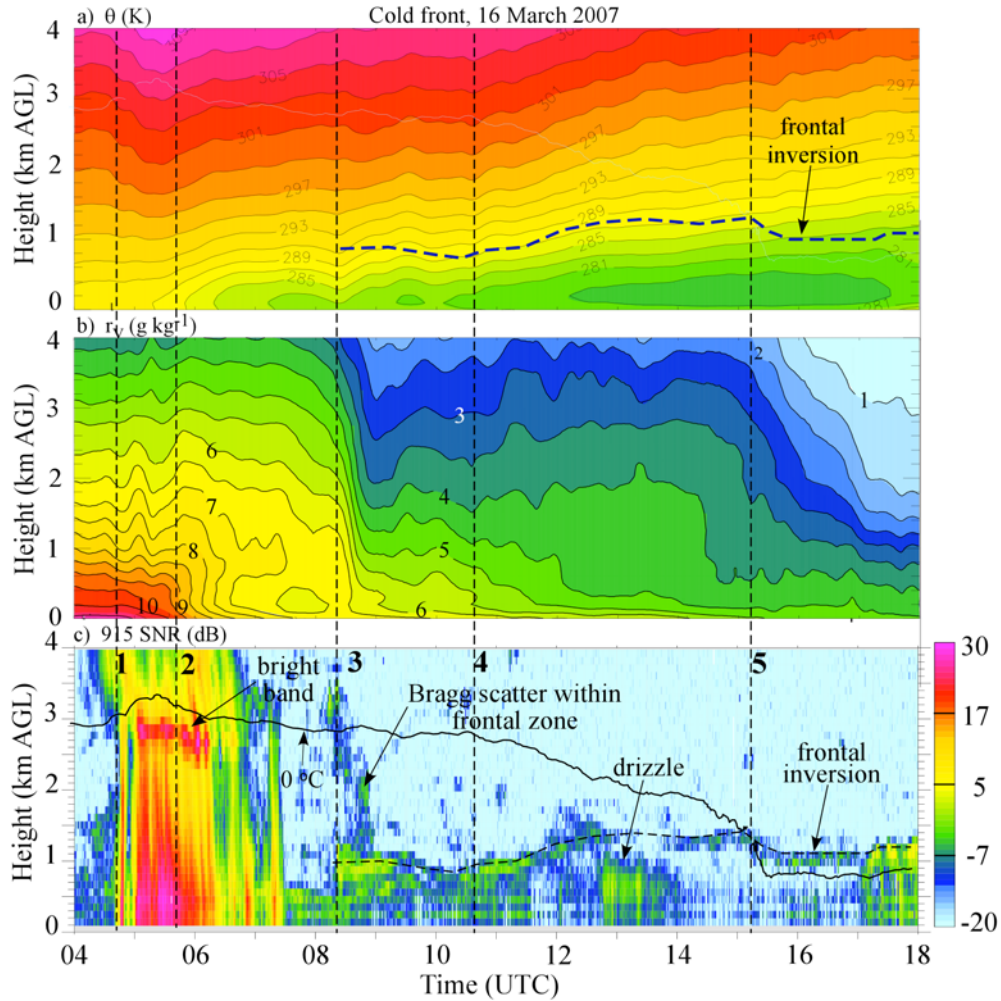


Figure 10. Time vs. height sections of parameters illustrating the passage of a cold frontal system on 16 March 2007. (a) MPR-derived potential temperature, contoured every 2 K, (b) MPR-derived mixing ratio, contoured every 0.5 g kg^{-1} , and (c) 915 MHz backscatter expressed in a signal-to-noise ratio (dB). Vertical lines labeled 1-5 refer to frontal features that are defined in the text. The frontal inversion, inferred from the 915 MHz SNR, is shown as a dashed line in panel c, and is overdrawn on the isentropes in panel a. The solid line in panel c represents the 0°C isotherm from the MPR retrieval. The warm bias produced by precipitation scattering and emission is represented by the upward protrusion of the isotherm above the bright band in panel c (between dashed lines 1 and 2).

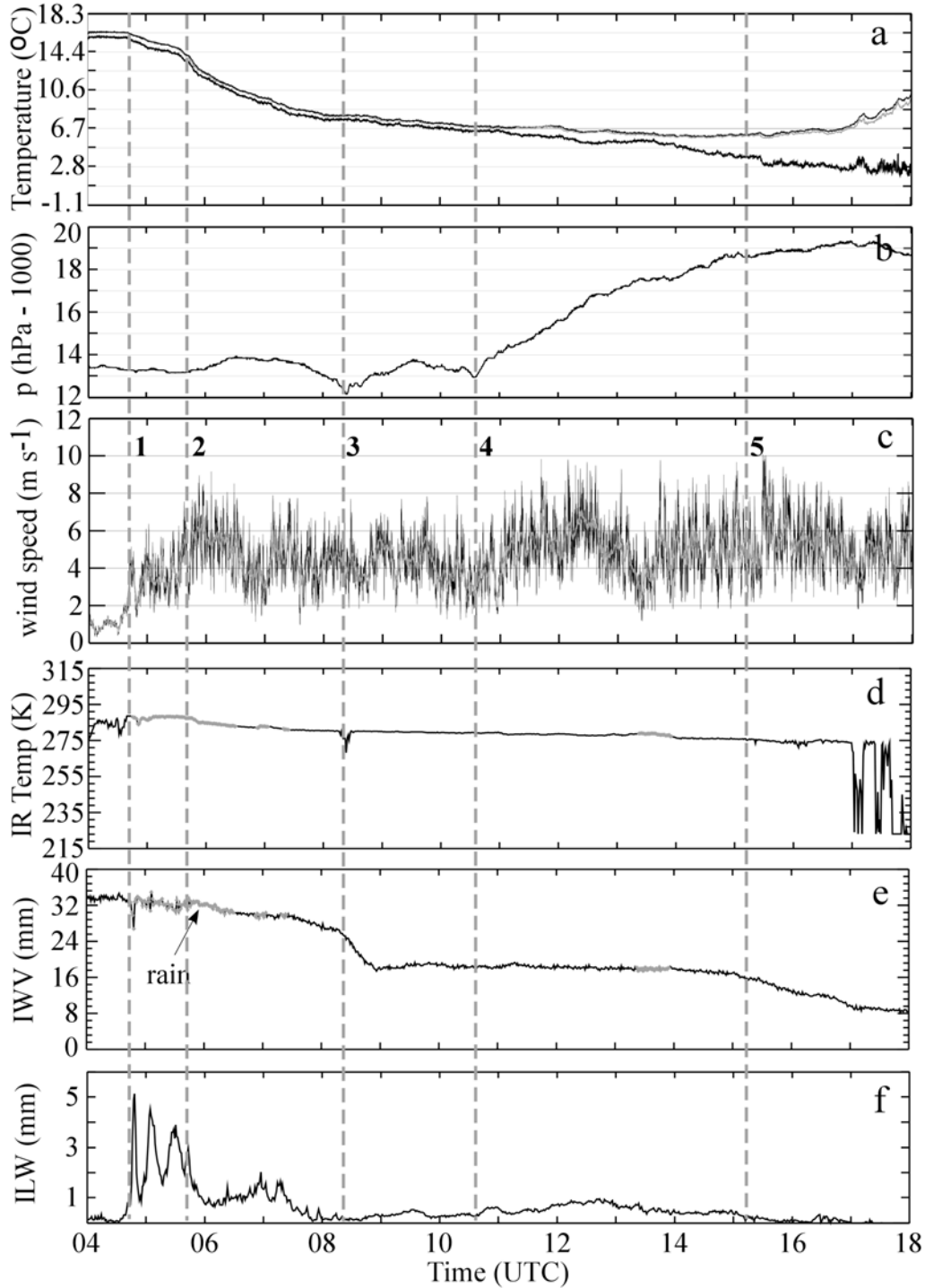


Figure 11. Time series of surface data (derived from independent surface instrumentation) and MPR data from the cold frontal system on 16 March 2007. Surface parameters include (a) temperature and dewpoint temperature, (b) pressure (reduced to sea-level), and (c) 10 m wind speed. MPR parameters include (d) IR temperature, (e) integrated water vapor (or precipitable water), and (f) integrated cloud water. The vertical dashed lines depict frontal gradients identified in Fig. 10.

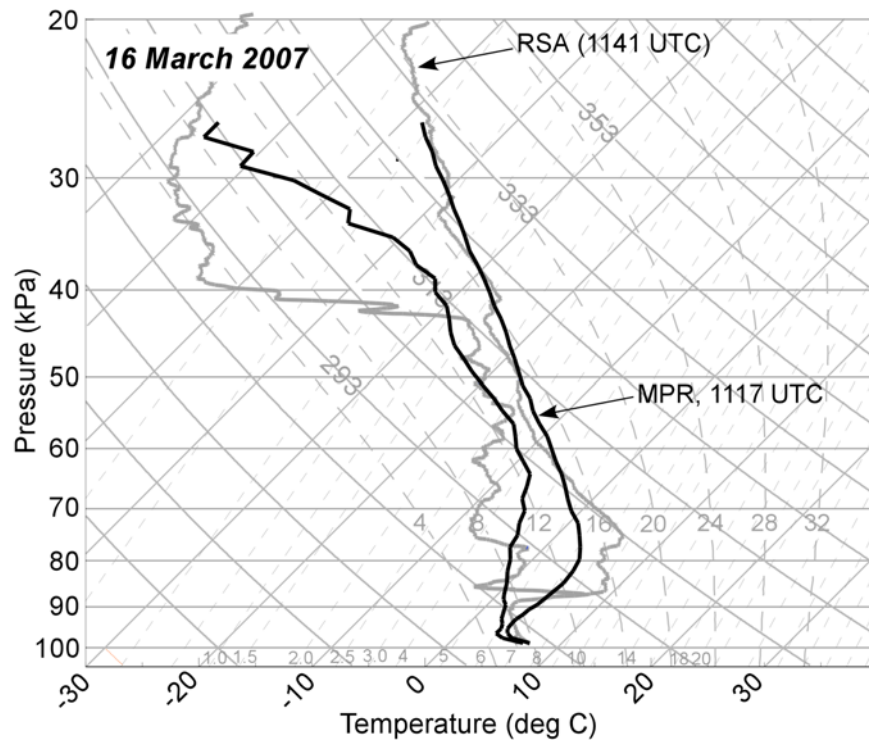


Figure 12. MPR and RSA soundings (16 March 2007 cold front), plotted on a skew-T, ln p diagram.

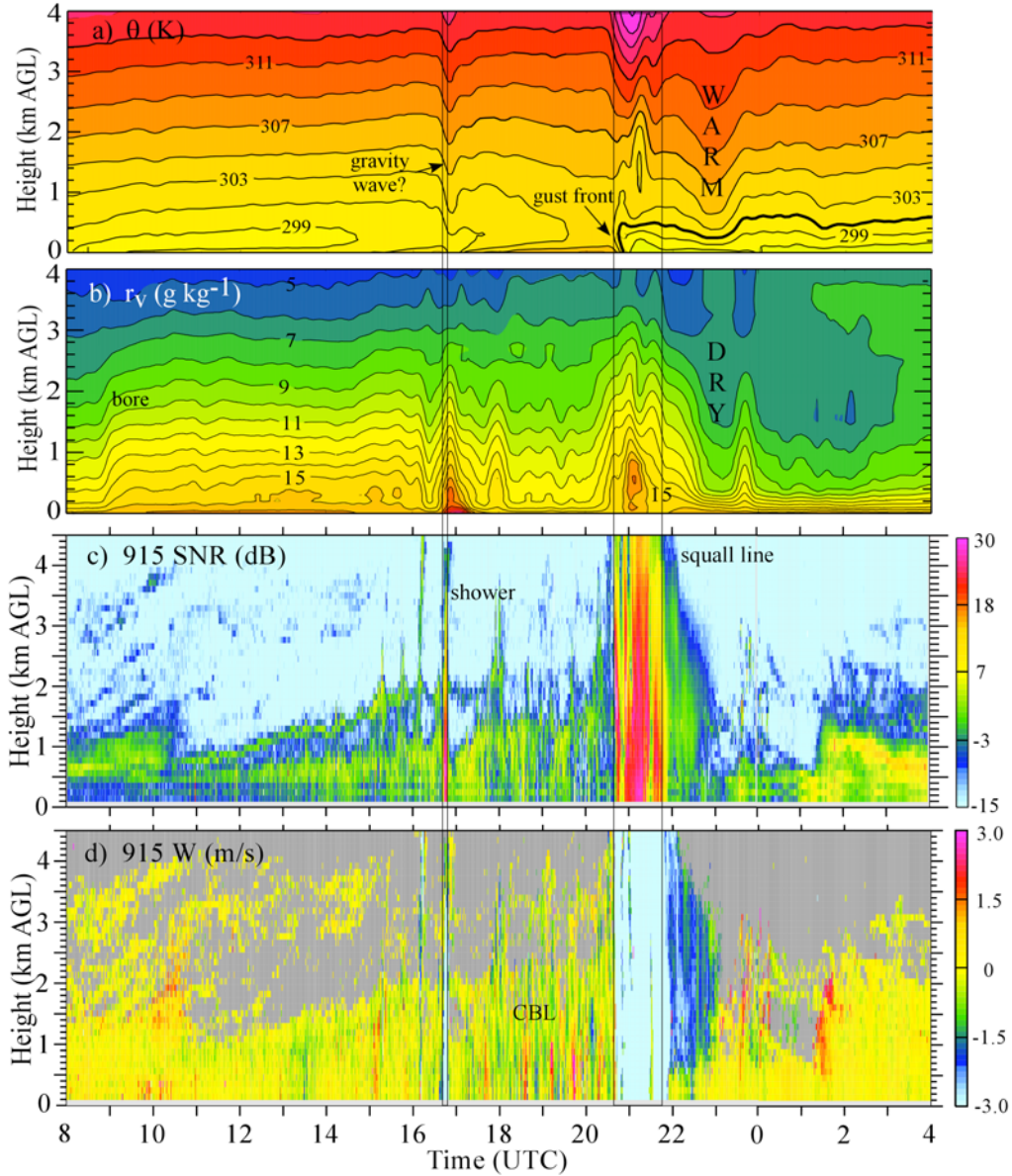


Figure 13. Time vs. height sections of parameters illustrating the pre-storm environment and the passage of a squall line on 8 June 2007. (a) MPR-derived potential temperature, contoured every 2 K, (b) MPR-derived mixing ratio, contoured every 0.5 g kg^{-1} , (c) 915 MHz backscatter expressed in a signal-to-noise ratio (dB), and (d) 915 MHz radial velocity from the vertical beam. The warm bias produced by precipitation scattering and emission is present in panels a and b (between vertical lines), but the low-level potential temperature appears to have experienced much lower bias. The 301 K isotherm is bold in panel a to depict the low-level density current.

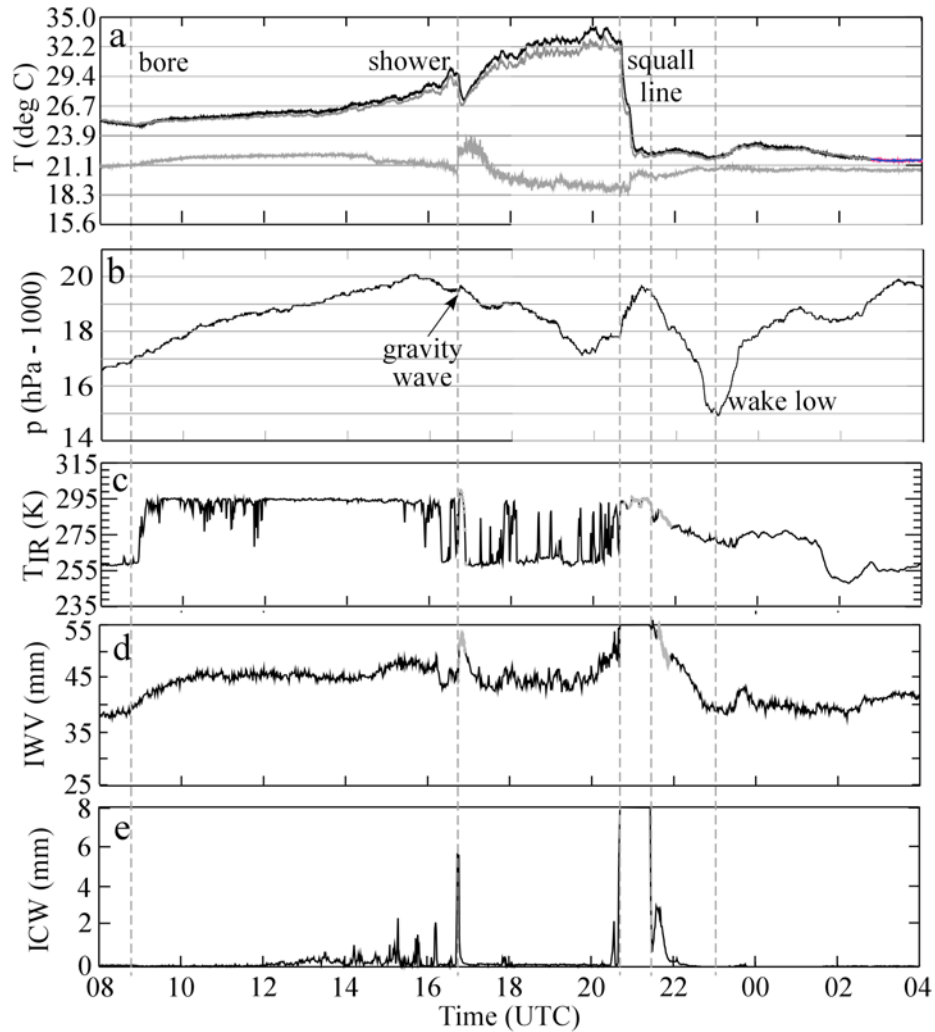


Figure 14. Time series of surface data (derived from independent surface instrumentation) and radiometer data from the 8 June 2007 squall line case. Surface parameters include (a) temperature and dewpoint temperature and (b) pressure (reduced to sea-level). MPR parameters include (c) IR temperature, (d) integrated water vapor (or precipitable water), and (e) integrated cloud water. The vertical dashed lines refer to significant features that are annotated in panels a and b.

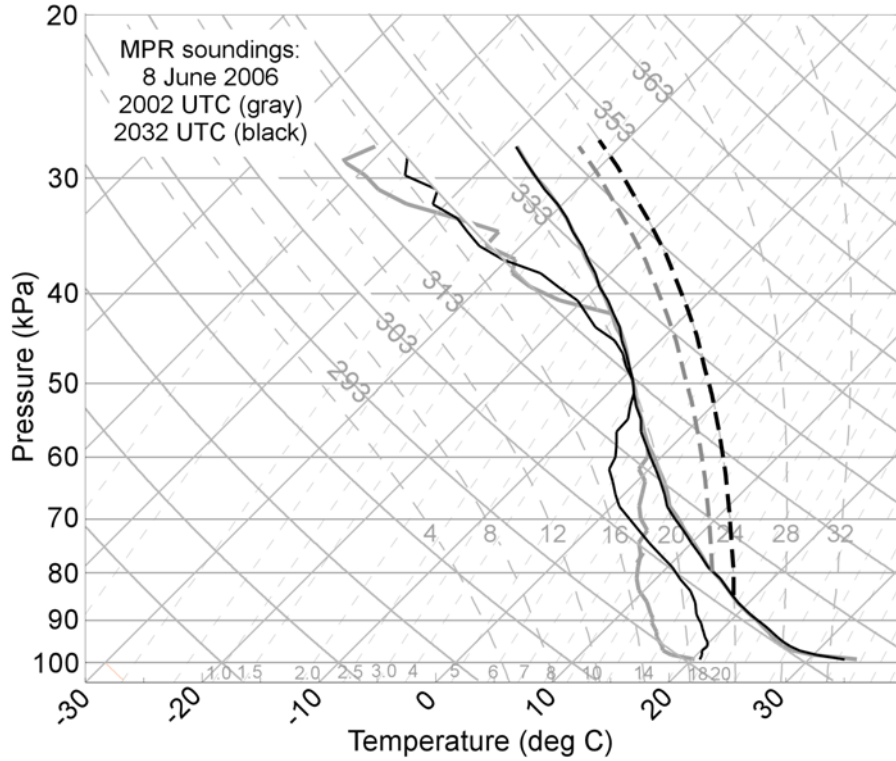


Figure 15. MPR soundings, plotted on a skew-T, ln p diagram. These soundings were sampled just in advance of the squall line and illustrate the rapid destabilization produced by an increase in low-level mixing ratio. Dashed lines represent saturated adiabats based on the lowest 50 mb average values of potential temperature and mixing ratio for each sounding.

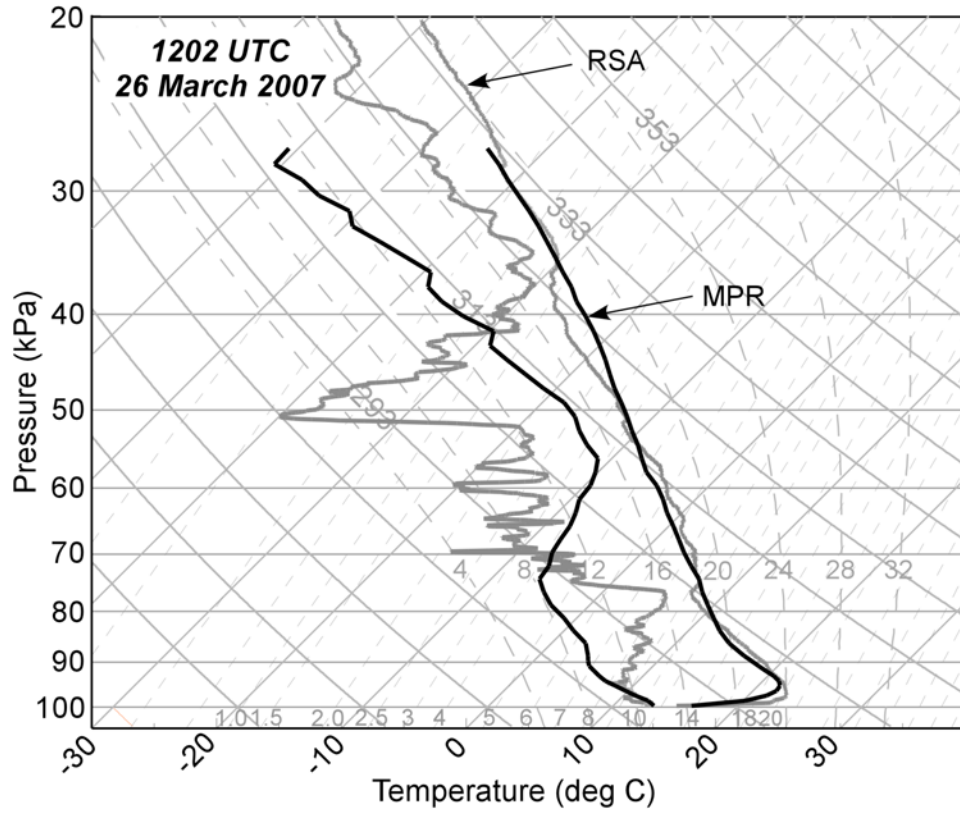


Figure 16. Nocturnal inversion soundings from the MPR and Redstone Arsenal (RSA) radiosonde at 1202 UTC on 26 March 2007.